

Imaging with Flat-Detector C-Arm Systems

NORBERT STROBEL, OLIVER MEISSNER, JAN BOESE, THOMAS BRUNNER, BENNO HEIGL, MARTIN HOHEISEL, GÜNTER LAURITSCH, MARKUS NAGEL, MARCUS PFISTER, ERNST-PETER RÜHRNSCHOPF, BERNHARD SCHOLZ, BERND SCHREIBER, MARTIN SPAHN, MICHAEL ZELLERHOFF and KLAUS KLINGENBECK-REGN

CONTENTS

3.1	Introduction	34
3.2	Technology of C-Arm CT Systems	34
3.2.1	C-Arm System Components	34
3.2.1.1	X-Ray Beam Generation and Exposure Control	34
3.2.1.2	Flat-Panel Detector Technology	34
3.2.1.3	C-Arm Gantries	35
3.2.2	C-Arm CT Image Acquisition and Dose	36
3.2.3	C-Arm CT and Image Quality	38
3.2.3.1	Cone-Beam Reconstruction Algorithm	38
3.2.3.2	Overexposure Correction	39
3.2.3.3	Scatter Correction	39
3.2.3.4	Beam Hardening Correction	40
3.2.3.5	Truncation Correction	41
3.2.3.6	Ring Artifact Correction	41
3.2.3.7	Image Quality	41
3.3	Applications	43
3.3.1	Interventional Imaging Using C-Arm CT	43
3.3.1.1	Neurovascular Imaging	43
3.3.1.2	Abdominal Imaging	44
3.3.1.3	Cardiac Imaging	45
3.3.2	Guidance of Interventional Procedures Using C-Arm CT	47
3.3.2.1	Enhanced X-Ray Navigation	47
3.3.2.2	Electromagnetic Navigation / Tracking (EMT)	48
3.4	Future Perspectives of C-Arm CT	48
	References	49

ABSTRACT

Three-dimensional (3D) C-arm computed tomography is a new and innovative imaging technique. It uses two-dimensional (2D) X-ray projections acquired with a flat-panel detector C-arm angiography system to generate CT-like images. To this end, the C-arm system performs a sweep around the patient, acquiring up to several hundred 2D views. They serve as input for 3D cone-beam reconstruction. Resulting voxel data sets can be visualized either as cross-sectional images or as 3D data sets using different volume rendering techniques. Initially targeted at 3D high-contrast neurovascular applications, 3D C-arm imaging has been continuously improved over the years and is now capable of providing CT-like soft-tissue image quality. In combination with 2D fluoroscopic or radiographic imaging, information provided by 3D C-arm imaging can be valuable for therapy planning, guidance, and outcome assessment all in the interventional suite.

N. STROBEL, PhD, O. MEISSNER, MD,
J. BOESE, PhD, T. BRUNNER, PhD, B. HEIGL, PhD,
M. HOHEISEL, PhD, G. LAURITSCH, PhD,
M. PFISTER, PhD, E.-P. RÜHRNSCHOPF,
B. SCHOLZ, PhD, B. SCHREIBER, PhD,
M. SPAHN, PhD, M. ZELLERHOFF, PhD,
and K. KLINGENBECK-REGN, PhD
Siemens AG, Healthcare Sector, MED AX, Siemensstrasse 1,
91301 Forchheim, Germany

M. NAGEL, PhD
CAS innovations, Heusteg 47, 91056 Erlangen, Germany

3.1

Introduction

Three-dimensional (3D) C-arm computed tomography is a new and innovative imaging technique. Also referred to as C-arm CT, it uses two-dimensional (2D) X-ray projection data acquired with flat-panel detector C-arm angiography systems to generate CT-like images (SAINT-FELIX et al. 1994; KOPPE et al. 1995; FAHRIG et al. 1997; BANI-HASHEMI et al. 1998; JAFFRAY and SEWERDSEN 2000; GROH et al. 2002; ZELLERHOFF et al. 2005; RITTER et al. 2007; KALENDER and KYRIAKU 2007). To obtain 2D radiographic projection data, the C-arm performs a sweep around the patient, e.g., over 200°. Up to several hundred images are acquired depending on the acquisition protocol selected. Reconstruction of three-dimensional voxel data sets from 2D raw projection data is performed using a 3D cone-beam reconstruction algorithm. Resulting voxel data sets can be visualized either as cross-sectional images or as 3D data sets using different volume rendering techniques.

Initially targeted at neuroendovascular imaging of contrast-enhanced vascular structures, 3D C-arm imaging has been continuously improved over the years. It is now capable of providing CT-like soft-tissue image quality directly in the interventional radiology suite. Beyond their use for trans-arterial catheter procedures, these 3D data sets are also valuable for guidance and optimization of percutaneous treatments such as liver tumor ablations. In combination with 2D fluoroscopic or radiographic imaging, information provided by 3D C-arm imaging can be very valuable for therapy planning, guidance, and outcome assessment—in particular for complicated interventions (MISSLER et al. 2000; ANXIONNAT et al. 2001; HERAN 2006; MEYER et al. 2007; WALLACE et al. 2007).

C-arm CT requires state-of-the-art C-arm systems equipped with flat-panel detector (FD) devices. It is commercially available from various vendors, e.g., marketed as *syngo* DynaCT (Siemens AG, Healthcare Sector, Forchheim, Germany), XperCT (Philips Healthcare, Andover, MA), or Innova CT (GE Healthcare, Chalfont St. Giles, UK).

The goal of this book chapter is to provide an overview of how 3D C-arm imaging works and for what it can be used. To this end, we focus on important C-arm system components first. Then we explain how X-ray input images are acquired and take a look at the resulting patient dose. In the next step, we cover three-dimensional image reconstruction and the correction methods needed to obtain low-contrast 3D results with CT-like image quality. After we explained how C-arm

CT images are generated, we analyze them in terms of spatial resolution and contrast resolution. In the remainder of this chapter, we look at clinical imaging results and C-arm CT applications including instrument guidance.

3.2

Technology of C-Arm CT Systems

3.2.1

C-Arm System Components

3.2.1.1

X-Ray Beam Generation and Exposure Control

The X-ray tube, X-ray generator, and X-ray control system are crucial components of any C-arm imaging system. They determine tube voltage, tube current, and irradiation time, respectively. These exposure parameters are essential for X-ray imaging, since contrast-detail perceptibility and dose depend on them.

Better contrast visibility, in particular of iodine, is the main reason why angiographic C-arm systems usually operate at lower tube voltages than CT scanners. Since decreasing tube voltage can lead to an increase in image noise, the question arises if better low contrast visibility at lower tube voltages can compensate for higher noise or not. Recent studies not only support this hypothesis, but they also indicate that there is great potential for dose reduction by scanning with lower tube voltages (MCCOLLOUGH 2005; NAKAYAMA et al. 2005).

The requirement to obtain high 2D image quality for fluoroscopic and radiographic imaging led to C-arm systems equipped with automatic exposure control (AEC). The use of AEC turns out to be extremely beneficial for C-arm CT imaging as well. In fact, it is very similar to attenuation-based tube current modulation used in CT. Tube current modulation can either improve image quality through noise reduction at a given dose, or it can reduce radiation exposure without impairing image quality (GIES et al. 1999; KALENDER et al. 1999).

3.2.1.2

Flat-Panel Detector Technology

Until the 1990s, C-arm systems for real-time angiographic imaging used to rely on X-ray image intensifiers (XRIIs). Although optimized over decades, this technology has a number of inherent disadvantages that

limit its utility for low-contrast C-arm CT imaging. For example, the convex input screen of XRIIs results in a non-homogeneous image quality across the output image. In addition, scatter processes of light and electrons within the image intensifier limit the coarse contrast resolution. This effect is also known as veiling glare (ROWLANDS and YORKSTON 2000). Yet another critical point with large image intensifier formats is patient access as well as the flexibility during angulation due to the large size of XRIIs.

Flat detectors, on the other hand, either avoid or at least reduce some of the major disadvantages of image intensifiers (GRANFORS et al. 2001; BRUIJNS et al. 2002; BUSSE et al. 2002; CHOQUETTE et al. 2001; COLBETH et al. 2001). The most important technical advantages of flat detectors are:

- Homogeneous image quality across the entire image area resulting in distortion-free images and position-independent spatial resolution.
- High 'low-contrast resolution,' i.e., good 2D soft-tissue imaging performance.
- High detective quantum efficiency (DQE) across all dose levels, in particular for CsI/aSi-based flat detectors.
- High dynamic range at all dose levels from fluoroscopy to digital subtraction angiography (DSA) facilitated by A/D converters with 14 bits.
- Tightly enclosed square or rectangular active imaging areas offering improved patient access.

The most widely used flat detector (FD) design is based on a two-level, indirect conversion process of X-rays to light (GRANFORS et al. 2001; ANTONUK et al. 1997; SPAHN et al. 2000; YAMAZAKI et al. 2004; DUCOURANT et al. 2003). In the first step, the X-ray quantum is absorbed by a fluorescence scintillator screen, e.g., a cesium iodide (CsI) substrate, converting it into visible light. In the second step, this light is received by a photodiode array, e.g., based on amorphous silicon (a-Si), and converted into electrical charge.

Besides good intrinsic X-ray absorption properties of the material itself, scintillator thickness is an important design parameter for X-ray detectors. A larger scintillator thickness improves the energy absorption efficiency and therefore the X-ray sensitivity of the detector. Unfortunately, it also reduces the spatial resolution due to optical diffusion blur. Thus, an optimum has to be found between X-ray sensitivity and spatial resolution. This is where CsI's columnar, needle-like microscopic crystalline structure provides a particular advantage. By limiting lateral optical light spread, CsI enables high spatial resolution at a larger phosphor thickness and, hence, increased X-ray sensitivity. As a result, CsI

is the scintillator material of choice for high-resolution X-ray applications at low dose levels. A typical value of the effective CsI scintillator thickness for FDs used in today's C-arm systems is around 500 μm .

A schematic view of an indirect converting flat detector based on CsI is presented in Fig. 3.1. An individual pixel is shown in detail, comprising a large photodiode and a small thin-film transistor (TFT). Pixel readout is initiated when the TFT is switched on. This causes the charge to flow to dedicated low-noise readout electronics, where it is amplified and subsequently converted into a digital signal.

Flat detector technology is subject to further development and continuous improvement. Miniaturized electronics will allow for even thinner and lighter detectors required for mobile or portable applications. Higher bit depths of 16 bits or even 18 bits will improve C-arm CT image quality, allowing it to further approach the low-contrast resolution of multi-slice computed tomography (MSCT).

3.2.1.3 C-Arm Gantries

An angiography device for 3D C-arm imaging comprises a stand and a C-arm to which the detector, X-ray tube, and collimator are attached. The C-arm keeps the X-ray tube, collimator, and flat-panel detector exactly aligned under varying view angles. Thanks to an open design maximizing the number of degrees of freedom

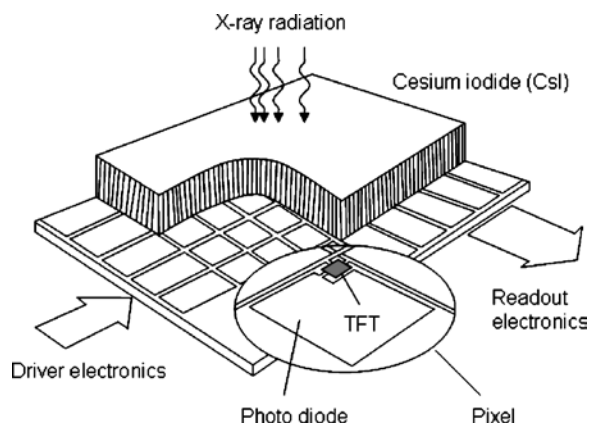


Fig. 3.1. Schematic view of an indirect converting flat detector based on CsI and an amorphous silicon active readout matrix, including driver and readout electronics. An individual pixel is shown in detail. It comprises a large photodiode and a small thin-film transistor (TFT)

for movements while minimizing the required space for the gantry itself, C-arm systems achieve high positioning flexibility and provide excellent patient access. As a result, C-arm systems are in use for interventional radiology, neuroradiology, cardiology, as well as for surgical applications.

In some cases, such as ceiling-mounted C-arm systems, the whole gantry can be rotated and translated to increase patient coverage and access. This traditional gantry design, shown in Fig. 3.2a, involves a mechanically fixed center of rotation commonly referred to as the isocenter. To further increase positioning flexibility, a new type of multi-axis C-arm system has recently been introduced (Artis **zeego**, Siemens AG, Healthcare Sector, Forchheim, Germany). Illustrated in Fig. 3.2b, this system involves a robotic stand moving a light-weight C-arm. Since the multi-axis stand facilitates greater flexibility, more accurate, faster movements, and better patient coverage, such systems are especially well suited for minimally invasive procedures and surgery.

3.2.2 C-Arm CT Image Acquisition and Dose

Although C-arm CT data acquisition is increasingly automated for ease of use, the following steps are usually involved. First, the patient needs to be optimally positioned such that the region of interest is visible in all

X-ray views acquired during a spin around the patient. With the patient properly placed, the C-arm is initially driven into a position, which will be the scan end position. Then a safety run is performed during which the C-arm is slowly moved into the actual C-arm CT start position. This safety run is required to rule out collision during the actual scan. After the C-arm has reached its start position, a short fluoroscopic X-ray pulse is applied to initialize the automatic exposure control. At this point, the system is ready to begin a 3D run during which the C-arm rotates from the start position into its end position. Raw data acquisition is performed by activating a dead-man switch. The rotational scan is stopped at once if the switch is released to prevent accidental X-ray exposure. On state-of-the-art C-arm CT systems, such as the Artis **zee** family (Siemens AG, Healthcare Sector, Forchheim, Germany), raw data acquisition and 3D reconstruction can be faster than 1 min depending on the scan protocol chosen.

Since C-arm CT is usually performed in an interventional setting, intra-arterial access is typically available. As a consequence, selective intra-arterial contrast injections can be used to enhance vessels as well as corresponding tissue regions during C-arm CT data acquisition.

X-ray input projections for C-arm CT can either be taken subtracted or native. Subtracted data acquisition involves a mask run without and a fill run after injection of contrast agent. Native data acquisition, on the other



Fig. 3.2a,b. C-arm gantries: An Artis **zee** ceiling-mounted C-arm (**a**) is shown on the *left*, while the Artis **zeego** (**b**) is depicted on the *right* (both Siemens AG, Healthcare Sector, Forchheim, Germany). The C-arm keeps the detector (posi-

tioned on *top*) exactly aligned with collimator and X-ray source (bottom-mounted). Detector and collimator rotate in synchronization as shown in (**b**). The X-ray source is built into the C-arm below the collimator

hand, involves only one set of input projections—often taken without (but conceivably also with) contrast.

C-arm CT systems with automatic exposure control (AEC) adjust X-ray exposure parameters such that the detector entrance dose remains constant. Detector entrance dose is the X-ray dose measured behind the antiscatter grid. System dose is the detector entrance dose evaluated at a reference detector zoom format. System dose is an important set-up parameter for C-arm CT imaging protocols on Artis **zee** systems (Siemens AG, Healthcare Sector, Forchheim, Germany). Due to internal adjustments, the detector entrance dose for C-arm CT is about half the system dose.

One way to monitor and report dose is to rely on an index such as the CT dose index (CTDI). A recent study investigating weighted CTDI (CTDI_w) and image quality for C-arm CT of the head demonstrated that the weighted CT dose index was within accepted limits (FAHRIG et al. 2006). Besides CTDI, the dose to the patient may also be quantified in terms of effective dose. For this purpose, anthropomorphic phantoms with embedded thermoluminescence detectors (TLDs) are used (BALTER et al. 2005). These phantoms have realistic body sizes and absorption values. Once the TLDs have been placed at selected positions inside a phantom, e.g., an Alderson phantom (Alderson Research Laboratories Inc., Long Island City, NY), it can be scanned using a particular C-arm CT examination protocol. The dose applied to single organs is derived by weighted summation of the individual TLD dose recordings. Effective dose is quantified in mSv instead of mGy. The worldwide average background dose for a human being is about 2.4 mSv per year (UNSCEAR 2000).

Although technical constraints and clinical requirements make it a non-trivial task to establish a practical set of clinical C-arm CT scan protocols, application-specific techniques can be established. This requires a careful choice of imaging parameters such as system dose, scan time, and pixel binning at the detector. Pixel binning means that the outputs of neighboring detector pixels are combined into one reading. For example, 2×2 binning implies that a total of four neighboring detector pixels that are adjacent in the horizontal and vertical direction, respectively, are taken together. Pixel binning determines spatial resolution, because it controls effective pixel size. The detector frame rate depends on pixel binning as well, because the amount of data is proportional to the number of pixels.

For C-arm CT data acquisition using an Artis **zee** system (Siemens AG, Healthcare Sector, Forchheim, Germany), the FD is mostly operated either in a 2×2 binning mode or in a 4×4 binning mode. For 2×2 binning, usually used for 3D C-arm imaging in the head,

we get a detector frame rate of 30 frames per second (fs^{-1}). In case of 4×4 binning, the frame rate increases to 60 fs^{-1} . The 4×4 binning mode is a clinically accepted setting for soft-tissue imaging in the abdomen, because it facilitates acquisition of a higher number of X-ray views in a shorter scan time.

Two sets of C-arm CT scan parameters and effective dose are presented below for Artis **zee** systems (Siemens AG, Healthcare Sector, Forchheim, Germany). They include mean effective dose values for the head and liver regions determined using a normal-size, male Alderson phantom with embedded TLDs. Since effective dose depends on phantom positioning and size, however, measurement outcomes may vary. This is why great care was taken to position the phantom identically for all experiments to obtain comparable results.

In Table 3.1, we summarize common high-contrast C-arm CT scan protocols and the resulting effective doses. These scan protocols are often used for subtracted runs involving injection of contrast agent to image vascular malformations such as aneurysms, arteriovenous malformations (AVMs), and stenoses. Tumor feeders can be visualized this way as well. Subtracted data acquisition is indicated in Table 3.1 by using a plus sign for the number of frames acquired. For 3D C-arm imaging where motion can be an issue, e.g., in the body, non-subtracted runs are usually the method of choice. Interventional imaging applications in the body that can benefit from C-arm CT include abdominal aortic aneurysms (AAAs), transjugular intrahepatic portosystemic shunts (TIPSs), non-vascular therapies, e.g., biliary duct treatments and tumors. The effective body dose stated in Table 3.1 was determined inside the liver region of an Alderson phantom using TLDs.

Table 3.2 lists two often-used scan parameter sets together with the resulting effective dose for low-contrast C-arm CT imaging in the head (therapy control, complication management) and in the body, e.g., for liver tumor treatment. Effective dose in the body was measured inside the liver region of an Alderson phantom using TLDs. A comprehensive list of C-arm CT scan protocols, including proper 3D reconstruction parameter settings for Artis **zee** systems (Siemens AG, Healthcare Sector, Forchheim, Germany), can be found in an application protocol book for these systems (MOORE and ROHM 2006).

Various adult effective doses for CT scans have been reported in the literature. For example, BECKER et al. (1998) obtained an effective dose of 6 mSv for a spiral scan of the abdomen. In a comprehensive review, MCCOLLOUGH and SCHUELER (2000) provide an effective dose between 1.9 mSv and 2.6 mSv for a (male) CT head scan and 7.3 mSv to 7.8 mSv for a (male) CT abdo-

Table 3.1. Common high-contrast C-arm CT scan protocols for Artis **zee** C-arm systems (Siemens AG, Healthcare Sector, Forchheim, Germany) and the resulting effective doses

Clinical application	System dose ($\mu\text{Gy}/\text{view}$)	Scan time (s)	Binning	No. frames	C-arm CT dose (mSv)
Head: vascular malformations, e.g., aneurysms, AVMs, stenoses, and tumor feeders	0.36	5	2×2	133 + 133	0.3
Body: AAA, TIPS, non-vascular therapies (e.g., biliary duct), and tumor feeders	0.36	5	2×2	133	1.5

Table 3.2. Common low-contrast C-arm CT scan protocols for Artis **zee** C-arm systems (Siemens AG, Healthcare Sector, Forchheim, Germany) and the resulting effective doses

Clinical application	System dose ($\mu\text{Gy}/\text{view}$)	Scan time (s)	Binning	No. frames	C-arm CT dose (mSv)
Head: therapy control, complication management	1.20	20	2×2	496	2
Body: liver tumor treatment	0.36	8	4×4	397	5

men scan, respectively. Comparing these values to the entries in Table 3.1 and Table 3.2, we see that high-contrast C-arm CT scan protocols result in a significantly lower dose to a patient, while the effective dose for a low-contrast C-arm CT examination appears similar to what is applied in regular CT scans.

3.2.3 C-Arm CT and Image Quality

3.2.3.1 Cone-Beam Reconstruction Algorithm

If C-arm systems can rotate around a patient along a sufficiently large angular scan range, then it is possible to use the acquired X-ray projections for tomographic image reconstruction. Usually a minimum angular scan range of 180° plus the so-called fan-angle is required (KAK and SLANEY 1999). For typical C-arm CT devices, this results in an angular scan range requirement of at least 200° .

In 1984, FELDKAMP et al. (1984) suggested a 3D reconstruction algorithm that has become the de-facto standard for 3D C-arm imaging. Originally designed

for a 360° scan along a perfectly circular trajectory, some modifications are, however, required before it can successfully process X-ray projections acquired along a C-arm CT scan trajectory. For example, a data weighting scheme is needed to compensate for the fact that during a partial circle scan some data are taken once, while other measurements are observed twice (PARKER 1982). In addition, a method may be needed with which to account for a C-arm system's irregular yet reproducible scan trajectory (ROUGEE et al. 1993; NAVAB et al. 1996; NAVAB et al. 1998; WIESENT et al. 2000).

Although predominately used for stationary objects, C-arm CT can also be applied to quasi-stationary 3D reconstruction problems, such as imaging the moving heart. To this end, the C-arm system performs multiple runs around the patient while the ECG signal is monitored. A continuous injection of contrast media is necessary to enhance the heart throughout data acquisition. The raw data obtained over the multiple runs can be resorted for a particular phase of the cardiac cycle using retrospective ECG gating. Since resorting of the acquired 2D X-ray views yields a valid input data set associated with the heart 'frozen' at a selected cardiac cycle, a standard C-arm CT reconstruction algorithm can be applied (LAURITSCH et al. 2006; PRUEMMER et al. 2007).

Sophisticated correction techniques are needed to obtain C-arm CT results with good low-contrast visibility. They are explained below. We start with overexposure correction, then turn to scatter correction, and next look into beam-hardening correction. After that, we briefly visit truncation correction and finish up with ring correction.

3.2.3.2 Overexposure Correction

While the dynamic range provided by 14-bit A/D converters of state-of-the-art flat-panel detectors is usually sufficient for conventional 2D fluoroscopic or radiographic imaging, it may not be high enough to rule out overexposure in all projections acquired during a C-arm CT scan. In this case, an object is X-rayed from many orientations. As a result, strong direct radiation may hit certain detector regions in some views and overexpose them.

Three-dimensional reconstruction from overexposed projections may result in incorrect density values and also produce a capping artifact. This means that gray values of a homogeneous object get increasingly smaller the further they are away from the object center. Since a capping artifact can impair the display of low-contrast objects, an overexposure correction is needed. It is applied to saturated image areas only. By correcting for overexposure, one may be able to obtain results without any apparent capping artifact.

3.2.3.3 Scatter Correction

Once overexposed image areas have been processed, scatter correction can be performed. Scattered X-ray quanta are photons that were deflected from their straight (primary) direction. They are detected at positions away from where a straight primary ray would hit the detector. As a result, the primary intensity distribution for tomographic reconstruction is impaired by a secondary distribution due to scattered radiation.

With single-row detectors of third generation CT scanners, scatter is almost negligible, because the irradiated patient volume is reduced to a small slice by collimation near the X-ray source. However, when working with flat-panel detectors, the collimator at the X-ray source is usually opened much more widely, and a considerable amount of scattered radiation may be produced. It can reach a multiple of the primary intensity in case of abdominal X-ray projections and up

to the order of magnitude of the primary intensity in head images (AICHINGER et al. 2004; SEWERDSEN and JAFFRAY 2001).

The impact of scatter on image quality is determined by the scatter-to-primary intensity ratio (SPR) at every detector pixel. Effective SPR reduction of up to about a factor of five can be obtained with anti-scatter grids (KYRIAKOU and KALENDER 2007). Unfortunately, even with an anti-scatter grid, scatter can still degrade image quality after tomographic reconstruction. Typical image quality problems caused by scatter are:

- Smooth gray value deviations within homogenous regions (cupping).
- Streaks, bars, or shadows in soft tissue regions, especially in the vicinity and between high contrast objects such as bones.
- Reduction of contrast differences in soft tissue regions.
- Increase of noise.

The appearance of cupping and shadowing artifacts due to scatter can be very similar to those created by beam hardening (RUEHRNSCHOPF and KALENDER 1981). Contrary to beam hardening, however, a decrease in differential contrast and an increase in noise are typical consequences of scatter.

Efficient scatter suppression and additional correction procedures are essential for C-arm CT to achieve CT-like image quality. A variety of scatter correction approaches exist. They comprise measurement techniques, software models, and hybrid approaches (NING et al. 2002; SEWERDSEN et al. 2006; ZHU et al. 2008). Since measurement techniques require additional hardware, software approaches are often preferable. Fast and efficient algorithms are available that operate directly on the projection images acquired (ZELLERHOFF et al. 2005; RINKEL et al. 2007). Iterative approaches appear promising to obtain further improvements beyond state-of-the-art scatter correction methods (KYRIAKOU et al. 2006).

The impact of scatter correction can be appreciated by looking at Fig. 3.3. As part of an overview illustrating the effect of C-arm CT correction methods provided by *syngo* DynaCT (Siemens AG, Healthcare Sector, Forchheim, Germany), we show an abdominal cross-section reconstructed without applying scatter correction in Fig. 3.3a. This data set suffers from a considerable cupping artifact. A reference result obtained after applying all correction steps is displayed in Fig. 3.3d. A comparison between Fig. 3.3a and Fig. 3.3d demonstrates that the cupping artifact due to scatter could be removed.

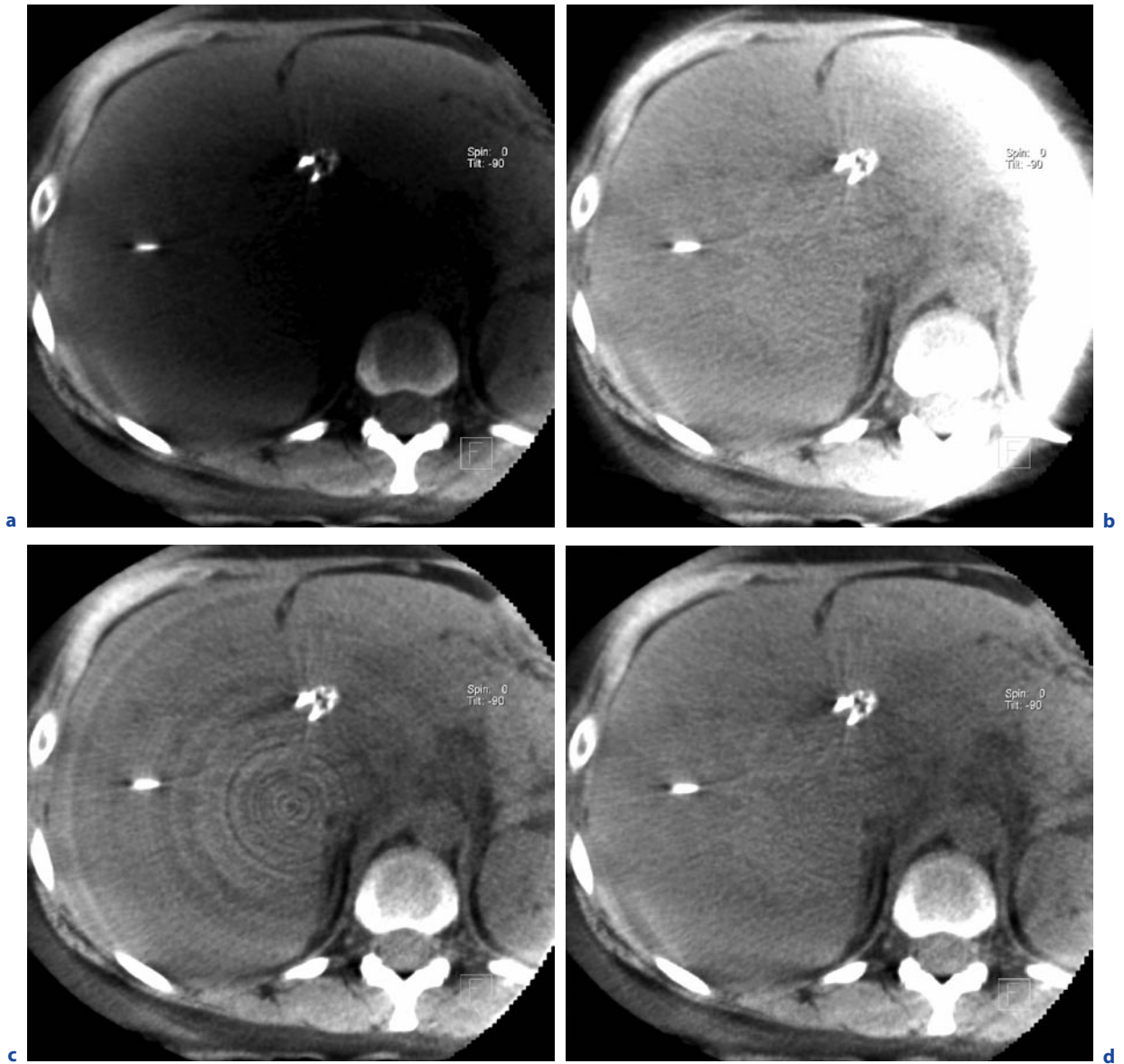


Fig. 3.3a–d. C-arm CT data sets computed using *syngo* DynaCT based on 2D X-ray projections acquired on an AXIOM Artis dTA system (both Siemens AG, Healthcare Sector, Forchheim, Germany) with correction techniques turned off/on. An axial abdominal slice without scatter correction is shown in (a). The same image reconstructed without truncation correction is

depicted in (b). Another result obtained without ring correction can be found in (c), and a reference section involving all correction steps is demonstrated in (d) (images courtesy of Dr. Loose and Dr. Adamus, Department of Radiology, Klinikum Nuremberg Nord, Germany)

3.2.3.4 Beam Hardening Correction

After dealing with overexposure and scatter removal, 2D projections can be corrected for beam hardening. X-ray tubes emit photons with different energies. Low-energy photons are absorbed and attenuated more strongly by matter than higher energy photons. As a consequence,

the mean energy of an X-ray beam's poly-energetic spectrum gets increasingly higher (harder) the further X-rays penetrate into an attenuating object. This physical effect is commonly referred to as beam hardening (BARRETT and SWINDELL 1981; HSIEH 2003).

Because of beam hardening, the linear relationship between attenuation value and object thickness no longer applies. As a result, attenuation values towards the

center of a large object may be underestimated, causing a cupping artifact. This means that density values for a homogeneous object get increasingly larger away from the center. In case of inhomogeneous objects, composed of tissue and bone, beam-hardening artifacts may also show up as streak artifacts between highly attenuating components, e.g., between bony structures surrounded by soft tissue.

The reduction of the two types of beam hardening artifacts requires two different correction approaches. The cupping artifact can be compensated by restoring a linear relationship between attenuation value and path length through an assumed water-equivalent object. This correction step, applied before carrying out any 3D reconstruction, is usually called ‘water correction.’ On the other hand, to reduce streak artifacts, one can make the assumption that the attenuating object is composed of water-equivalent tissue and bones and then design an algorithm to correct for beam hardening caused by the two different materials (JOSEPH and SPITAL 1978).

3.2.3.5 Truncation Correction

Unlike in MSCT systems, where detectors are usually wide enough to always capture a patient’s full X-ray profile irrespective of view direction, FDs of today’s C-arm systems may not be large enough to accomplish this in any case. As a result, it is possible that X-ray projections are truncated in some or even all views. Truncated projections can be problematic for tomographic reconstruction algorithms, because they may generate bright circular artifacts and result in incorrectly reconstructed density values as shown in Fig. 3.3b.

Truncation artifacts and density errors can be reduced by applying row-wise extrapolation techniques (OHNESORGE et al. 2000; STARMAN et al. 2005; SOURBELLE et al. 2005; ZELLERHOFF et al. 2005; HSIEH et al. 2004). Since row-wise extrapolation only depends on neighboring data in a horizontal direction, this approach is adaptive, and it can be very effective, as shown in Fig. 3.3d.

New multi-axis C-arm gantry designs, such as the Artis **zeego** (Siemens AG, Healthcare Sector, Forchheim, Germany) shown in Fig. 3.2b, can be operated in a large-volume scan mode. This approach almost doubles the object size that can be reconstructed without truncation artifacts, because two C-arm runs are performed with the detector positioned such that it captures one half of an X-ray projection in one run while recording the remaining half in the other.

3.2.3.6 Ring Artifact Correction

Ring artifacts are caused by detector gain inhomogeneities or defective detector pixels. Fortunately, elaborate detector calibration and built-in FD defect correction can usually correct detector pixel problems to a large extent, thus preventing most serious ring artifacts right at the detector.

Nevertheless, with the steadily improving image quality of C-arm CT, even the slightest 3D image imperfections start to show up. This is why a ring correction algorithm is needed. Implemented as a post-processing algorithm, it first generates a ring image using sophisticated image processing techniques. This ring image is then subtracted from the initial reconstruction result to obtain a cleaned-up image as depicted in Fig. 3.3c and Fig. 3.3d (FLOHR 2000; ZELLERHOFF et al. 2005).

3.2.3.7 Image Quality

Thanks to a detector optimized for high-resolution 2D fluoroscopic and radiographic imaging, the spatial resolution provided by C-arm CT can be very high. For example, a common FD for large-plate C-arm systems, such as the 30 cm × 40 cm Pixium 4700 flat-panel detector (Trixell, Moirans, France), offers a native pixel pitch of 154 μm in a 1,920 × 2,480 matrix. Although this leads to an excellent spatial resolution, taking full advantage of it reduces the FD frame rate in overview mode to 7.5 fs⁻¹. Such a low frame rate limits its clinical use to certain high-contrast applications unless special read-out techniques are applied. Higher frame rates are possible by applying 2 × 2 binning or 4 × 4 binning of detector pixels. Since pixel binning combines neighboring detector elements, the effective pixel width and height increases to 308 μm (2 × 2 binning) or to 616 μm (4 × 4 binning), respectively.

To arrive at a first estimate of how detector pixel width is related to spatial resolution, let us start with an example based on a detector pixel pitch of 308 μm. This is the pixel width of the Pixium 4700 FD when operated in 2 × 2 binning mode. Taking into account a cone-beam magnification factor between isocenter and detector of 1.5, we arrive at an effective pixel size at isocenter of 205 μm. This suggests that a spatial (in-plane) resolution of up to 2.4 LP/mm should be achievable after tomographic reconstruction (1/0.410 mm), if imaging conditions were ideal. Unfortunately, additional factors such as finite focal spot size, gantry motion, and 3D reconstruction kernel may lower spatial resolution. For

example, the spatial resolution after tomographic reconstruction for an Artis **zee** system using *syngo* DynaCT (both Siemens AG, Healthcare Sector, Forchheim, Germany) is not 2.4 LP/mm as estimated above, but rather 2.0 LP/mm as depicted in Fig. 3.4. The smallest high contrast object that can be resolved at 2.0 LP/mm has a size of about 250 μm or 0.25 mm. At native detector resolution (154 μm pixel pitch), the spatial resolution encountered in phantom measurements reaches almost 4.0 LP/mm. This means that details may be resolved that are as small as 0.13 mm. If 4×4 binning is applied, then the spatial resolution seen in bar-pattern experiments is about 1.0 LP/mm, i.e., the system can be expected to resolve objects with a size of around 0.50 mm. This value is only slightly less than results obtained with current multi-slice CT devices. In fact, the 4×4 binning mode is a clinically well accepted acquisition technique for low-contrast C-arm CT imaging, e.g., in the abdomen, because the increased detector frame rate enables the acquisition of a higher number of views in a shorter time frame. The higher number of views results in improved low-contrast detectability, while the shorter scan

time reduces the chance of artifacts due to patient motion, breathing, or peristalsis.

Contrast resolution characterizes a C-arm CT system's capacity to resolve soft tissue differences. For good low-contrast imaging results, it is advantageous to acquire a high number of views, because this reduces streak artifacts. To further reduce noise in applications such as head scans, an additional option may be to increase system dose.

With a properly selected image acquisition protocol, state-of-the-art C-arm CT systems such as *syngo* DynaCT (Siemens AG, Healthcare Sector, Forchheim, Germany) can at least resolve 5-mm (10-mm) diameter objects with a contrast difference of 10 HU (5HU) (FAHRIG et al. 2006). Even better results are sometimes possible as demonstrated in Fig. 3.5. From a clinical point of view, the low-contrast imaging performance of today's C-arm systems not only can be expected to differentiate between fat and muscle tissue, but C-arm CT can also resolve smaller contrast differences and possibly even visualize bleeds.

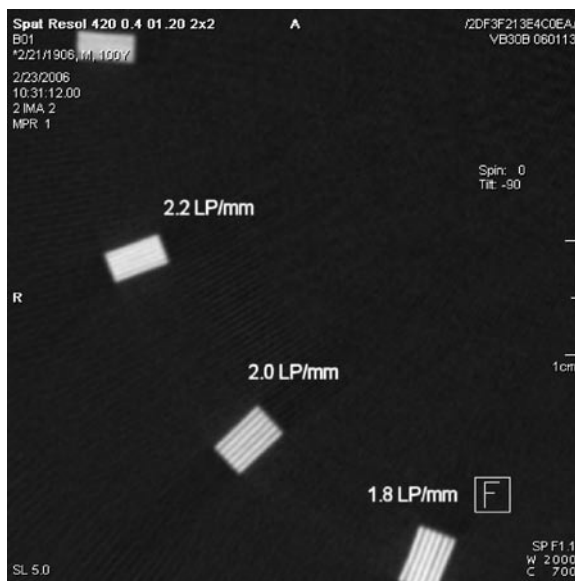


Fig. 3.4. Spatial resolution experiment involving an axial slice through a spatial resolution phantom. The 3D spatial resolution from 2D X-ray projections acquired with a Trixell Pixium 4700 detector is about 2.0 LP/mm, if 2×2 -pixel binning is applied. Projection data were acquired on an Artis **zee** C-arm system, and reconstruction was performed with *syngo* DynaCT (both Siemens AG, Healthcare Sector, Forchheim, Germany)

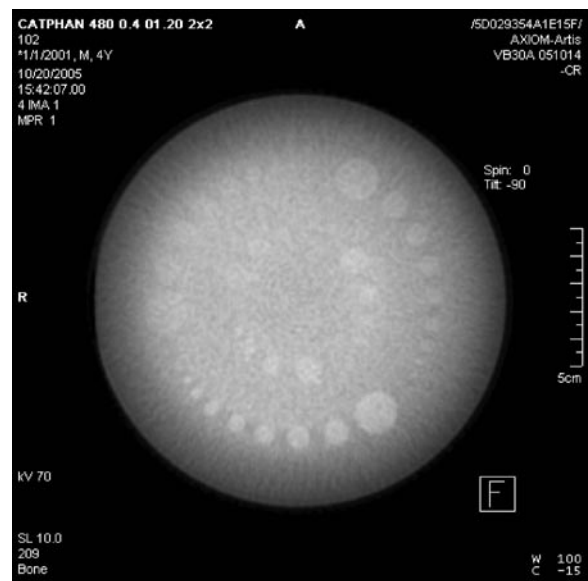


Fig. 3.5. C-arm CT reconstruction of the CTP515 CATPHAN image quality segment (Phantom Laboratory, Salem, NY) using *syngo* DynaCT (Siemens AG, Healthcare Sector, Forchheim, Germany). A 10-mm-thick MPR slice is shown. It comprises low-contrast-equivalent insets with a density difference of 10 HU (5 o'clock to 8 o'clock), 5 HU (1 o'clock to 4 o'clock), and 3 HU (9 o'clock to 12 o'clock). The diameters of the individual insets are 15, 9, 8, 7, 6, 5, 4, 3, and 2 mm, respectively. The 3D data set was reconstructed from 538 raw input projections acquired on an Artis **zee** system at 70 kV tube voltage (Siemens AG, Healthcare Sector, Forchheim, Germany). The associated weighted CT dose index (CTDI_w) was 50 mGy

3.3

Applications

3.3.1

Interventional Imaging Using C-Arm CT

3.3.1.1

Neurovascular Imaging

Two-dimensional digital subtraction angiography (DSA) is still considered a gold-standard imaging technique for diagnostic and therapeutic imaging of intracranial vessels. One of DSA's advantages is its superb spatial resolution. Today, however, many clinicians often rely on 3D C-arm imaging as well—at least for complex cases. In fact, several studies comparing 2D DSA to 3D C-arm imaging concluded that 3D images can offer more detailed anatomical information for the therapy of intracranial aneurysms than 2D DSA (Hoff et al. 1994; Tu et al. 1996; Missler et al. 2000; Sugahara et al. 2002; Hochmuth et al. 2002). In addition to providing more information about the aneurysm neck, the available 3D geometry can also be used to find optimal C-arm working views (Anxionnat et al. 2001; Mitschke and Navab

2000). This is illustrated in Fig. 3.6 for a lobulated intracranial aneurysm. Once a proper view orientation has been found by interactively inspecting a rendered volume, the C-arm can be automatically positioned at the selected view angle for 2D imaging. On *syngo* X-workplace systems (Siemens AG, Healthcare Sector, Forchheim, Germany), a little blue icon is used to denote C-arm positions that can be reached safely. A red icon indicates that the C-arm cannot be aligned with a certain volume-rendered view due to collision control or mechanical constraints.

When using 3D C-arm imaging for the visualization of stents, physicians again found that access to 3D information during the intervention facilitated better clinical outcomes (VAN DEN BERG et al. 2002; BENNDORF et al. 2005, 2006; RICHTER et al. 2007a). BENNDORF et al., for example, valued the clear visualization of both the stent struts and their adaptation to arterial walls and aneurismal lumen.

Another important C-arm CT application in the brain is tumor imaging. For example, intra-arterially contrast-enhanced 3D C-arm imaging can reveal both vascularity and blood supply of a meningioma of the olfactory groove, as illustrated in Fig. 3.7a–c. An axial slice is displayed in Fig. 3.7a, a sagittal cross-section is

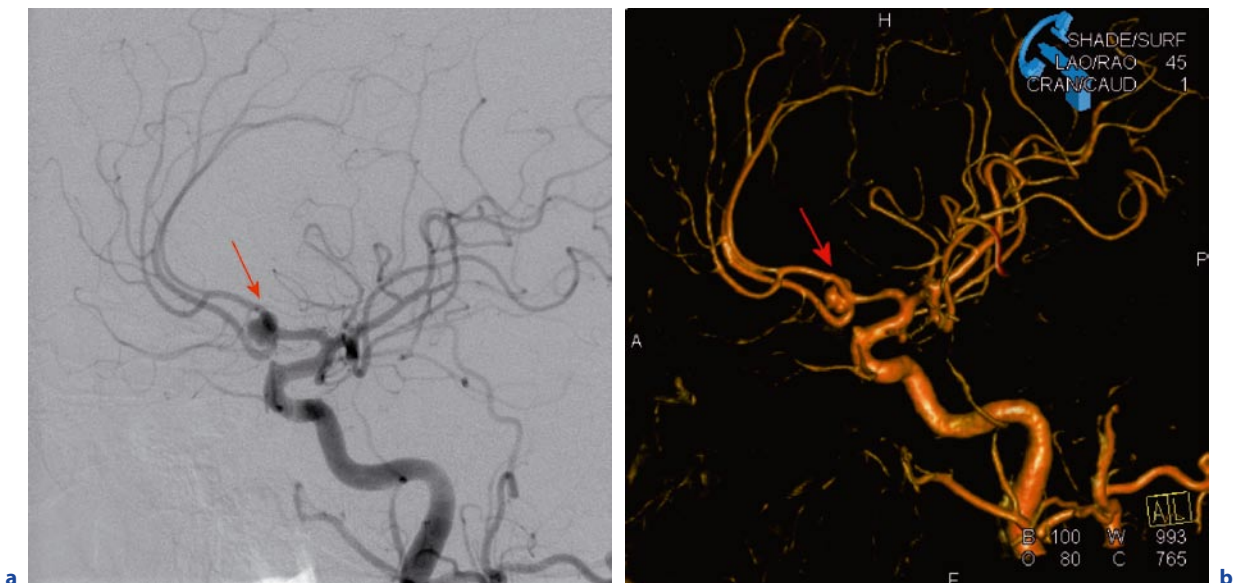


Fig. 3.6a,b. View-aligned DSA and C-arm CT data sets. C-arm systems can be brought into proper 2D working views by rendering a 3D data set interactively under various orientations, choosing the most suitable view, and initiating an automatic C-arm move. This is displayed for a DSA sequence (**a**) and a volume rerendered 3D vessel tree (**b**) depicting a lobulated intracranial aneurysm (red arrow). Images were acquired

on an AXIOM Artis dBA system and reconstructed on a *syngo* X-workplace running *syngo* DynaCT (all Siemens AG, Healthcare Sector, Forchheim, Germany). DSA sequence and 3D vessel tree are both seen under LAO/RAO = 45° and CRAN/CAUD = 1° (images courtesy of Prof. Knauth, Department of Neuroradiology, University Göttingen, Germany)

shown in Fig. 3.7b, and a coronal cut through the lesion can be found in Fig. 3.7c, respectively. A volume rendered display is presented in Fig. 3.7d. This information can be useful to determine the best treatment option. The C-arm CT images were obtained with *syngo* DynaCT running on a *syngo* X-workplace (both Siemens AG, Healthcare Sector, Forchheim, Germany). X-ray projections were acquired on an AXIOM Artis dBA angiography system (Siemens AG, Healthcare Sector, Forchheim, Germany).

3.3.1.2 Abdominal Imaging

Besides endovascular treatments in the brain, C-arm CT is also well suited to support abdominal applications. In fact, C-arm CT has already received considerable attention for minimally invasive liver tumor treatments. Innovative therapeutic approaches, such as local chemotherapy, chemoembolization, or selective internal radiation therapy (SIRT), may all benefit,

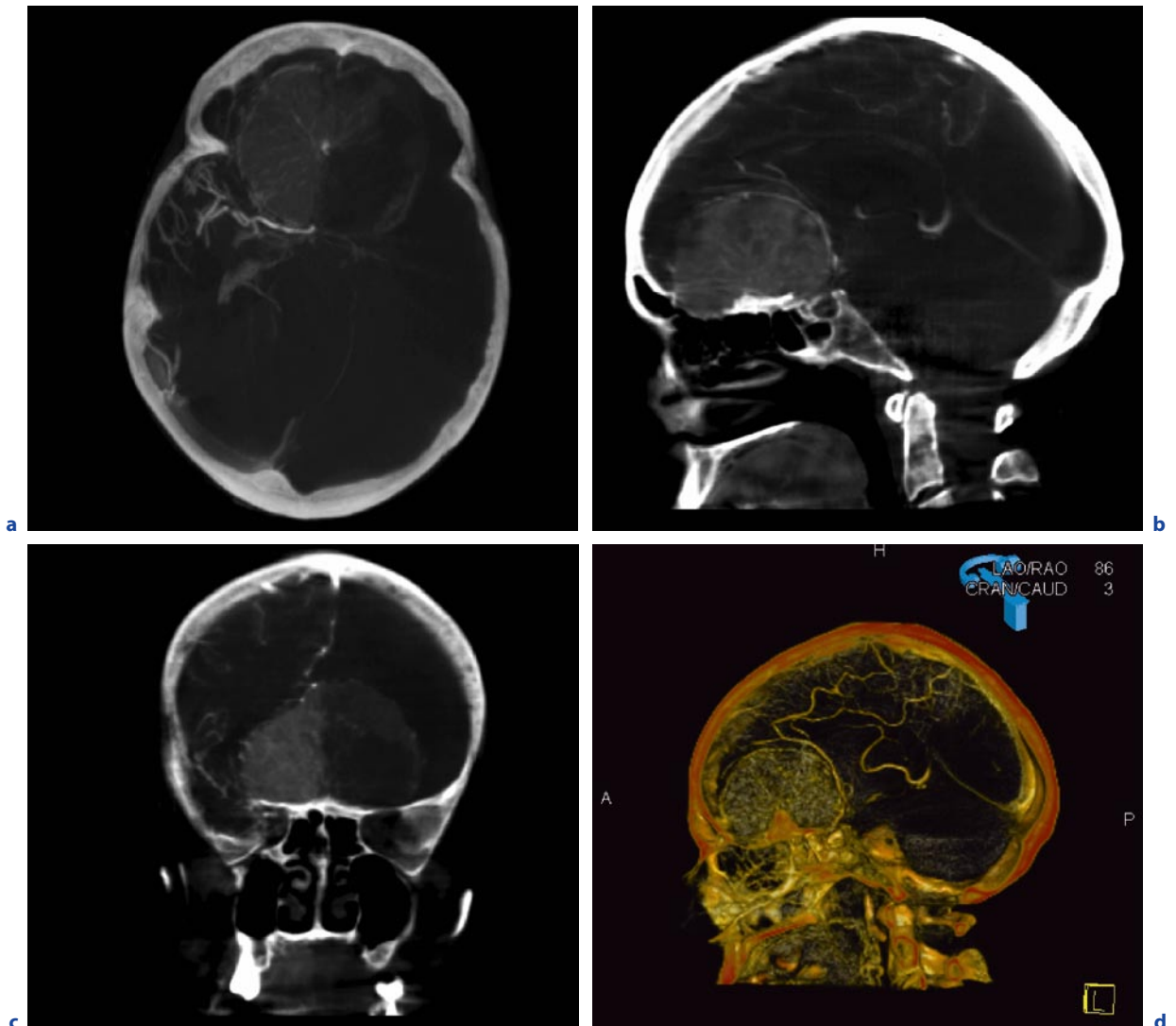


Fig. 3.7a–d. C-arm CT images showing a meningioma of the olfactory groove: axial (a), sagittal (b), coronal cross-section (c), and volume rendered display (d). The C-arm CT results were obtained with *syngo* DynaCT running on a *syngo* X-workplace (both Siemens AG, Healthcare Sector, Forchheim,

Germany). X-ray projections were acquired on an AXIOM Artis dBA angiography system (images courtesy of Prof. Doerfler, Department of Neuroradiology, University Erlangen-Nuremberg, Germany)

because C-arm CT can be used to image both feeder vessels and soft tissue. For example, MEYER et al. recently presented five cases involving abdominal transarterial chemoembolization in which C-arm CT had a considerable impact on the course of the treatment (MEYER et al. 2007). Based on their experience, MEYER et al. (2007) concluded that C-arm CT has the potential to expedite any interventional procedure that requires three-dimensional information and navigation. Similarly, WALLACE et al. (2007) found that C-arm CT

provided additional imaging information beyond DSA in approximately 60% of all cases. In about 19% of all procedures, procedure management changed. When VIRMANI et al. (2007) investigated the usefulness of C-arm CT for transcatheter arterial chemoembolization (TACE) of unresectable liver tumors, they observed that 3D C-arm imaging led to different catheter positions in 39% of all cases, while improving the diagnostic confidence in 78% of all patients.

Another procedure that can benefit from 2D and 3D X-ray imaging is uterine fibroid embolization. In addition to 2D fluoroscopic imaging for catheter guidance, C-arm CT can confirm blood supply to fibroids in 3D as well. This is illustrated in Fig. 3.8. Data sets were generated on an Artis **zeego** system (Siemens AG, Healthcare Sector, Forchheim, Germany). Figure 3.8a was obtained with the catheter in the left uterine artery revealing blood supply to two fibroids. Figure 3.8a also demonstrates single-run C-arm CT volume coverage. Figure 3.8b, on the other hand, was acquired using Artis **zeego**'s large-volume scan mode involving two scans with the detector positioned such that it captures one half of an X-ray projection in one run and the remaining half in the other. For this data set, the catheter was placed in the right uterine artery to confirm if it also supplies blood to the fibroids or not. The Artis **zeego**'s large-volume C-arm CT imaging mode increases the width of the field-of-view from 25 cm, displayed in Fig. 3.8a, to 47 cm, illustrated in Fig. 3.8b. Figure 3.8b demonstrates that large-volume *syngo* DynaCT (Siemens AG, Healthcare Sector, Forchheim, Germany) provides superior organ coverage.

Additional clinical applications in the body that can benefit from C-arm CT are drainages and punctures. When performing percutaneous biliary drainage procedures, FROEHLICH et al. (2000), for example, found that C-arm CT resulted in decreased procedure and fluoroscopy times. C-arm CT can also be beneficial for complicated transjugular intrahepatic portosystemic shunt cases (SZE et al. 2006). BINKERT et al. (2006) described another successful application for C-arm devices providing both 2D and 3D imaging. They used the 3D cross-sectional information for needle placement and 2D fluoroscopy to perform embolization of translumbar type II endoleaks.

3.3.1.3 Cardiac Imaging

Cardiac imaging for electrophysiology treatments is another promising field for C-arm CT imaging. It can provide accurate morphological information in the in-

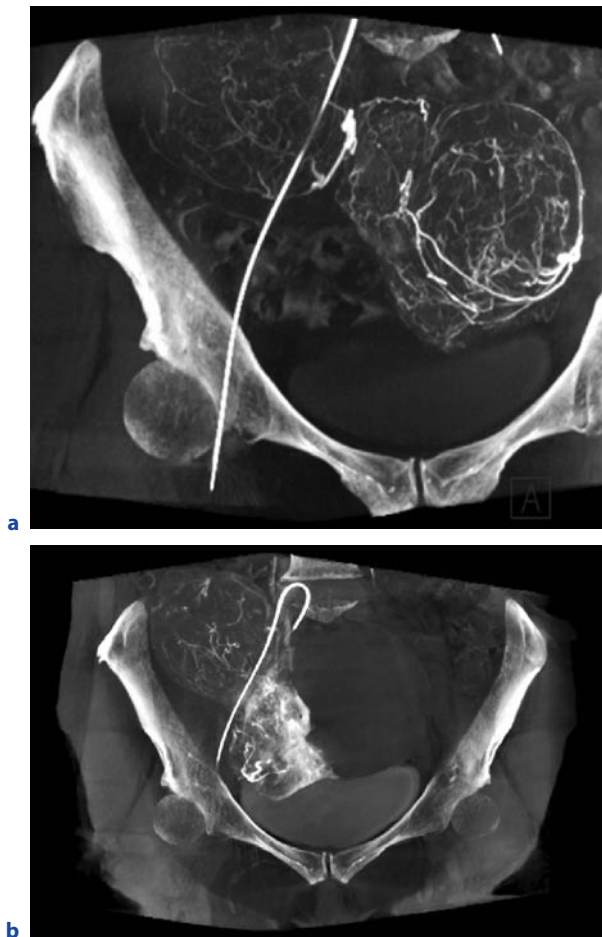


Fig. 3.8a,b. Uterine fibroid embolization. A maximum-intensity-projection (MIP) image of a C-arm CT data set obtained with the catheter in the left uterine artery is shown in (a). Another MIP image with the catheter in the right uterine artery is displayed in (b). Results were obtained with an Artis **zeego** multi-axis C-arm system (Siemens AG, Healthcare Sector, Forchheim, Germany) using the regular C-arm CT data acquisition mode (a) and the large-volume mode (b) (images courtesy of Dr. Waggerhauser, Department of Clinical Radiology, University of Munich, Germany)

terventional suite immediately before, during, and after an ablation procedure, whereas preoperative CT images may be limited in accuracy due to changes in anatomical heart structures over time.

First clinical results obtained with *syngo* DynaCT Cardiac (Siemens AG, Healthcare Sector, Forchheim, Germany) are shown in Fig. 3.9a–d. Three multiplanar reformatted images are displayed with a slice thickness of 2.1 mm. They illustrate important anatomical struc-

tures, such as the four heart chambers (Fig. 3.9a) and the left ventricle together with the ascending aorta and the aortic valve (Fig. 3.9b). In this case, even a coronary artery could be successfully imaged, as shown in Fig. 3.9c. A volume rendered posterior view of the contrast-enhanced heart is displayed in Fig. 3.9d. There, the esophagus was enhanced using barium (see yellow arrow) to obtain information about its position relative to the left atrium.



Fig. 3.9a–d. Multiplanar reformatted images (MPRs) reconstructed using an ECG-based multi-segment C-arm CT technique such as *syngo* DynaCT Cardiac (Siemens AG, Healthcare Sector, Forchheim, Germany). Images are rendered with a slice thickness of 2.1 mm. A four-chamber view is shown in the upper left (a). The left ventricle, ascending aorta, and aortic valve

can be found in the upper right (b). In the lower left, the proximal right coronary artery is depicted (c). A volume rendered posterior 3D view of the contrast-enhanced heart is displayed in the lower right (d). The yellow arrow points to the barium-enhanced esophagus (images courtesy of Prof. Brachmann and Dr. Nölker, Klinikum Coburg, Germany)

3.3.2 Guidance of Interventional Procedures Using C-Arm CT

In the past, image guidance in the interventional suite has been limited to 2D X-ray fluoroscopic imaging. With the emergence of C-arm CT, however, it is now possible to generate 3D data sets and perform real-time 2D imaging in the same room without having to relocate the patient.

3.3.2.1 Enhanced X-Ray Navigation

Two-dimensional fluoroscopic images, which are usually acquired to guide interventional procedures at very low X-ray dose, offer excellent spatial and temporal resolution. Unfortunately, fluoroscopic images lack both contrast resolution and 3D information. This may cause difficulties when localizing devices with respect to treatment regions. Three-dimensional C-arm CT data sets, on the other hand, can provide both low-contrast resolution and a 3D spatial orientation, but not in real-time. By integrating 2D fluoroscopic imaging with 3D C-arm CT, the strengths of both methods can be combined. The result is an auto-registered (hybrid) system integrating 2D and 3D X-ray imaging.

Since 2D and 3D imaging modalities are mechanically coregistered, 3D C-arm CT data sets can be used for (augmented) real-time visualization of 2D fluoroscopic projections (RICHTER et al. 2007b). This is illustrated in Fig. 3.10. Figure 3.10a depicts a 3D vascular segment (in red) overlaid onto a coiled aneurysm. Fig. 3.10b shows a volume-rendered roadmap with vessels (in light orange) to facilitate guidewire navigation. Since a volume-rendered roadmap can be recomputed in real-time, changes in C-arm viewing angles, source-detector-distance, zoom, and table movements can all be taken into account without any need to acquire another 2D roadmap. From a clinical point of view, volume-rendered roadmapping can reduce the amount of contrast medium administered to a patient and lessen X-ray dose. It can also save some procedure time (SOEDERMAN et al. 2005).

Live 2D fluoroscopy augmented with anatomical overlays derived from C-arm CT data sets can be further enhanced by including an additional treatment plan for instrument guidance. Such a plan can be generated by annotating a C-arm CT data set, e.g., by adding points and drawing lines. This treatment plan can then be superimposed on 2D X-ray projections either together with an anatomical overlay or even without it. Similar to anatomical overlays, the 2D appearance of a treatment plan set up in 3D is also updated whenever the C-arm view orientation changes. This way, an appropriate



Fig. 3.10a,b. Enhanced X-ray navigation: Scene (a) depicts a 3D vascular segment (in red) overlaid onto a coiled aneurysm. Scene (b) shows a volume-rendered roadmap with vessels (in orange). Both results were generated with *syngo* iPilot (Siemens

AG, Healthcare Sector, Forchheim, Germany) (images courtesy of Prof. Mawad, Baylor College of Medicine, Department of Radiology, Houston, TX)

overlay view of both anatomy and treatment plan can be obtained under each C-arm projection angle.

An interesting clinical application that can benefit from the use of graphical treatment plans is percutaneous needle guidance. The advantage of using a C-arm system for percutaneous needle procedures is superior access to bigger patients and better support for complex, double-oblique needle trajectories. To set up a treatment plan, the physician specifies a target point and a needle trajectory in 3D first. To this end, a C-arm CT data set may be used. In the next step, the C-arm is moved into a bull's eye view (down-the-barrel view) that aligns X-ray view orientation and needle path. This view orientation is used to insert the needle. After the needle has been placed, the C-arm is driven back and forth between two suitably chosen progression views to monitor needle advancement. If needed, C-arm CT data sets can be generated throughout the procedure to confirm the needle position in 3D. If a thin slice is sufficient, narrow collimation may be preferable as it reduces patient dose. Needle guidance for C-arm systems is commercially available as iGuide (Siemens AG, Healthcare Sector, Forchheim, Germany) or XperGuide (Philips Healthcare, Andover, MA).

One challenge for X-ray guidance involving C-arm CT volume data is that the relation between the 3D data sets and the 2D projection images needs to be maintained at all times. This requires stabilizing or tracking the patient. However, if misalignment does occur, then 2D-3D registration algorithms are available to correct for it (BYRNE et al. 2004; BAERT et al. 2004; PRUEMMER et al. 2006).

3.3.2.2 Electromagnetic Navigation / Tracking (EMT)

Electromagnetic (EM) tracking (EMT) systems receive an increasing amount of attention in interventional radiology. These tracking systems use a transmitter located in the vicinity of the patient. It houses several coils generating a complex EM field that extends to some 50 cm in front of the device. If a small coil (position sensor) is brought into the EM field, the voltage induced can be used to calculate sensor position and orientation. With modern systems, a position accuracy of around 1 mm can be achieved. Position sensors are usually located in the tip of interventional instruments, e.g., needles used for biopsy, drainage, vertebroplasty, or radiofrequency ablation devices.

The workflow of an electromagnetically navigated intervention is as follows. First, the patient is placed on the table of the C-arm CT system possibly immobilized



Fig. 3.11. Typical setup of an electromagnetic (EM) navigation system. The transmitter, held by the flexible arm shown in the center of the image, is placed underneath sterile covers. Since the needle has an integrated localization sensor, the tracking system can show its position inside a registered C-arm CT data set. The 3D data was generated with an AXIOM Artis dBA C-arm system (Siemens AG, Healthcare Sector, Forchheim, Germany), while EM navigation was performed with a CAPPa IRAD EMT navigation system (CAS innovations, Erlangen, Germany) (image courtesy of Prof. Wacker, Charité, Berlin, Germany)

using a vacuum mattress. In the next step, a C-arm CT data set is generated. Afterwards, the C-arm CT data set is registered to the coordinate system of the tracking device. Different registration methods exist depending on the EM tracking system used (NAGEL et al. 2007). After registration, the EM tracking system can display real-time instrument movement within a C-arm CT data set using a graphical instrument representation as shown in Fig. 3.11. It is also possible to mark target and skin entry point in the 3D data set and, based on this information, use EMT to navigate the needle to the desired position. Initial clinical results obtained for percutaneous procedures have demonstrated that EM navigation based on C-arm CT data sets can be safe and effective (NAGEL et al. 2008).

3.4 Future Perspectives of C-Arm CT

The technical progress in C-arm CT is going to continue. In fact, the recently introduced Artis **zeego** system (Siemens AG, Healthcare Sector, Forchheim, Germany) already provides a glimpse into the future of advanced C-arm devices. Based on a new multi-axis platform

combined with a light-weight C-arm, these systems are not only going to offer better patient access, but they will also support faster, more flexible image acquisition trajectories for increased 3D coverage. Latest C-arm gantry designs together with further optimized X-ray generation components, more advanced flat detectors, and increasingly sophisticated 3D reconstruction algorithms will improve C-arm CT image quality beyond what is currently available. Since navigation techniques and instruments are continuously upgraded as well, it seems safe to predict that future C-arm systems are going to be integrated medical devices seamlessly combining high-quality C-arm CT with 2D live imaging and device navigation for therapy planning, guidance, and outcome assessment all in the interventional suite.

Acknowledgements

We would like to thank Angelika Hench and Sabine Wich for their help with the clinical image data sets.

References

- Aichinger H, Dierker J, Joite-Barfuß S, et al. (2004) Radiation exposure and image quality in X-ray diagnostic radiology-Physical principles and clinical applications. Springer, Heidelberg Berlin New York
- Antonuk LE, El-Mohri Y, Siewerdsen JH, et al. (1997) Empirical investigation of the signal performance of a high-resolution, indirect detection, active matrix flat-panel imager (AMFPI) for fluoroscopic and radiographic operation. *Med Phys* 24 :51–70
- Anxionnat R, Bracard S, Ducrocq X, et al. (2001) Intracranial aneurysms: Clinical value of 3D digital subtraction angiography in the therapeutic decision and endovascular treatment. *Radiology* 218:799–808
- Baert SAM, Penney GP, van Walsum T, et al. (2004) Precalibration versus 2D-3D registration for 3D guide wire display in endovascular interventions. In: *Medical Image Computing and Computer-Assisted Intervention—MICCAI*, pp 577–584
- Balter S, Banckwitz R, Joite-Barfuß S, et al. (2005) Protocol for evaluating CT reconstructions acquired on an angiographic C-arm. *Biomedizinische Technik* 50 (Suppl 1, part 1):475–476
- Bani-Hashemi A, Navab N, Nadar M, et al. (1998) Interventional 3D-angiography: calibration, reconstruction and visualization system. In: Navab N (ed) *Fourth IEEE Workshop on Applications of Computer Vision*, 1998. WACV '98. Proceedings, pp. 246–247
- Barrett HH, Swindell W (1981) *Radiological Imaging*. Academic Press, New York
- Becker CR, Schätzl M, Feist H, et al. (1998) Radiation dose for investigation of the chest and abdomen. Comparison of sequential, spiral and electron beam computed tomography. *Radiologe* 38:726–729
- Benndorf G, Strother CM, Claus B, et al. (2005) Angiographic CT in cerebrovascular stenting. *Am J Neuroradiol* 26:1813–1818
- Benndorf G, Klucznik RP, Strother CM (2006) Angiographic computed tomography for imaging of underdeployed intracranial stent. *Circulation* 114 :499–500
- Binkert CA, Alencar H, Singh J, et al. (2006) Translumbar type II endoleak repair using angiographic CT. *J Vasc Intervent Radiol* 17:1349–1353
- Bruijns TJC, Bastiaens RJM, Hoornaert B, et al. (2002) Image quality of a large-area dynamic flat detector: comparison with a state-of-the-art II/TV system. In: *Medical Imaging 2002: Physics of Medical Imaging*. San Diego, pp 332–343
- Busse F, Ruetten W, Sandkamp B, et al. (2002) Design and performance of a high-quality cardiac flat detector. In: *Medical Imaging 2002: Physics of Medical Imaging*. San Diego, CA, pp 819–827
- Byrne JV, Colominas C, Hipwell J, et al. (2004) Assessment of a technique for 2D-3D registration of cerebral intra-arterial angiography. *Br J Radiol* 77:123–128
- Choquette M, Demers Y, Shukri Z, et al. (2001) Performance of a real-time selenium-based X-ray detector for fluoroscopy. In: *Medical Imaging 2001: Physics of Medical Imaging*. San Diego, CA, pp 501–508
- Colbeth RE, Boyce SJ, Fong R, et al. (2001) 40×30 cm flat-panel imager for angiography, R&F, and cone-beam CT applications. In: *Medical Imaging 2001: Physics of Medical Imaging*. San Diego, CA, pp 94–102
- Ducourant T, Couder D, Wirth T, et al. (2003) Image quality of digital radiography using flat detector technology. In: *Medical Imaging 2003: Physics of Medical Imaging*. San Diego, CA, pp 203–214
- Fahrig R, Fox AJ, Lownie S, et al. (1997) Use of a C-arm system to generate true three-dimensional computed rotational angiograms: preliminary in vitro and in vivo results. *Am J Neuroradiol* 18:1507–1514
- Fahrig R, Dixon R, Payne T, et al. (2006) Dose and image quality for a cone-beam C-arm CT system. *Med Phys* 33:4541–4550
- Feldkamp L, Davis L, Kress J (1984) Practical cone-beam algorithm. *J Opt Soc Am A* 1:612–619
- Flohr T (2000) Method for post-processing of a tomogram and computed tomography apparatus operating in accordance with the method. US Patent 6047039, Siemens AG, Germany
- Froelich JJ, Wagner H-J, Ishaque N, et al. (2000) Comparison of C-arm CT fluoroscopy and conventional fluoroscopy for percutaneous biliary drainage procedures. *J Vasc Intervent Radiol* 11:477–482
- Gies M, Kalender WA, Wolf H, et al. (1999) Dose reduction in CT by anatomically adapted tube current modulation. I. Simulation studies. *Med Phys* 26:2235–2247

- Granfors PR, Albagli D, Tkaczyk JE, et al. (2001) Performance of a flat-panel cardiac detector. In: *Medical Imaging 2001: Physics of Medical Imaging*. San Diego, CA, pp 77–86
- Groh BA, Siewerdsen JH, Drake DG, et al. (2002) A performance comparison of flat-panel imager-based MV and kV cone-beam CT. *Med Phys* 29:967–975
- Heran NS, Song JK, Namba K, et al. (2006) The Utility of DynaCT in neuroendovascular procedures. *A J Neuroradiol* 27:330–332
- Hochmuth A, Spetzger U, Schumacher M (2002) Comparison of three-dimensional rotational angiography with digital subtraction angiography in the assessment of ruptured cerebral aneurysms. *Am J Neuroradiol* 23:1199–1205
- Hoff DJ, Wallace MC, terBrugge KG, et al. (1994) Rotational angiography assessment of cerebral aneurysms. *Am J Neuroradiol* 15:1945–1948
- Hsieh J (2003) *Computed Tomography*. SPIE Press, Bellingham, WA
- Hsieh J, Chao E, Thibault J, et al. (2004) A novel reconstruction algorithm to extend the CT scan field-of-view. *Med Phys* 31:2385–2391
- Jaffray DA, Siewerdsen JH (2000) Cone-beam computed tomography with a flat-panel imager: Initial performance characterization. *Med Phys* 27:1311–1323
- Joseph PM, Spital RD (1978) A method for correcting bone-induced artifacts in computed tomography scanners. *J Comp Ass Tomography* 2:100–108
- Kalender W, Wolf H, Suess C (1999) Dose reduction in CT by anatomically adapted tube current modulation. II. Phantom measurements. *Med Phys* 26:2248–2253
- Kalender W, Kyriakou Y (2007) Flat-detector computed tomography (FD-CT). *Eur Radiol* 17:2767–2779
- Kak AC, Slaney M (1988) *Principles of Computerized Tomographic Imaging*. IEEE, New York
- Koppe R, Klotz E, de Beek JO, et al. (1995) Three-dimensional vessel reconstruction based on rotational angiography. In: Lemke HU, Inamura K, Jaffe CC, et al. (eds) *Proc Int Symp Computer Assisted Radiology*. Springer, Berlin Heidelberg New York, pp 101–107
- Kyriakou Y, Riedel T, Kalender W (2006) Combining deterministic and Monte Carlo calculations for fast estimation of scatter intensities in CT. *Phys Med Biol* 51:4567–4586
- Kyriakou Y, Kalender W (2007) Efficiency of antiscatter grids for flat-detector CT. *Phys Med Biol* 52:6275–6293
- Lauritsch G, Boese J, Wigstrom L, et al. (2006) Towards cardiac C-arm computed tomography. *IEEE Transact Med Imaging* 25:922–934
- McCollough CH, Schueler BA (2000) Calculation of effective dose. *Med Phys* 27:828–837
- McCollough CH (2005) Automatic exposure control in CT: Are we done yet? *Radiology* 237:755–756
- Meyer B, Frericks B, Albrecht T, et al. (2007) Contrast-enhanced abdominal angiographic CT for intra-abdominal tumor embolization: A new tool for vessel and soft tissue visualization. *Cardiovasc Intervent Radiol* 30:743–749
- Missler U, Hundt C, Wiesmann M, et al. (2000) Three-dimensional reconstructed rotational digital subtraction angiography in planning treatment of intracranial aneurysms. *Eur Radiol* 10:564–568
- Mitschke MM, Navab N (2000) Recovering projection geometry: How a cheap camera can outperform an expensive stereo system. *CVPR 2000*:1193–1200
- Moore T, Rohm E (2006) *Application protocol book for Artis zee 3D applications*. Siemens AG
- Nagel M, Hoheisel M, Petzold R, et al. (2007) Needle and catheter navigation using electromagnetic tracking for computer-assisted C-arm CT interventions. In: *Medical Imaging 2007: Visualization and Image-Guided Procedures*. San Diego, CA, pp 65090J
- Nagel M, Hoheisel M, Bill U, et al. (2008) Electromagnetic tracking system for minimal invasive interventions using a C-arm system with CT option: First clinical results. In: *Medical Imaging 2008: Visualization and Image-Guided Procedures*. San Diego, CA, pp 69180G
- Nakayama Y, Awai K, Funama Y et al. (2005) Abdominal CT with low tube voltage: Preliminary observations about radiation dose, contrast enhancement, image quality, and noise. *Radiology* 237:945–951
- Navab N, Bani-Hashemi AR, Mitschke MM, et al. (1996) Dynamic geometrical calibration for 3D cerebral angiography. In: *Medical Imaging 1996: Physics of Medical Imaging*. Newport Beach, CA, pp 361–370
- Navab N, Bani-Hashemi A, Nadar M, et al. (1998) Three-dimensional reconstruction from projection matrices in a C-arm based 3D-angiography system. In: *Medical image computing and computer-assisted intervention—MICCAI'98*, pp 119–129
- Ning R, Tang X, Conover DL (2002) X-ray scatter suppression algorithm for cone-beam volume CT. In: *Medical Imaging 2002: Physics of Medical Imaging*. San Diego, CA, pp 774–781
- Ohnesorge B, Flohr T, Schwarz K, et al. (2000) Efficient correction for CT image artifacts caused by objects extending outside the scan field of view. *Med Phys* 27:39–46
- Parker D (1982) Optimal short scan convolution for fanbeam CT. *Med Phys* 9:254–257
- Pruemmer M, Hornegger J, Pfister M, et al. (2006) Multimodal 2D-3D non-rigid registration. In: *Medical Imaging 2006: Image Processing*. San Diego, CA, pp 61440–61412
- Pruemmer M, Fahrig R, Wigstrom L, et al. (2007) Cardiac C-arm CT: 4D non-model based heart motion estimation and its application. In: *Medical Imaging 2007: Physics of Medical Imaging*. San Diego, CA, pp 651015–651012
- Richter G, Engelhorn T, Struffert T, et al. (2007a) Flat panel detector angiographic CT for stent-assisted coil embolization of broad-based cerebral aneurysms. *Am J Neuroradiol* 28:1902–1908

- Richter G, Pfister M, Struffert T, et al. (2007b) Visualization of self-expandable stents using 2D-3D coregistration of angiographic computed tomography data to facilitate stent assisted coil embolization of broad based intracranial aneurysms: in vitro feasibility study. In: 42. Jahrestagung der Deutschen Gesellschaft für Neuroradiologie, Frankfurt am Main
- Rinkel J, Gerfault L, Esteve F, et al. (2007) A new method for X-ray scatter correction: First assessment on a cone-beam CT experimental setup. *Phys Med Biol* 52:4633–4652
- Ritter D, Orman J, Schmidgunst C, et al. (2007) Three-dimensional soft tissue imaging with a mobile C-arm. *Comput Med Imaging Graphics* 31:91–102
- Rowlands JA, Yorkston J (2000) Flat panel detectors for digital radiography. In: Metter RLV, Beutel J, Kundel HL (eds) *Handbook of Medical Imaging*. SPIE Press, Bellingham, WA, pp 223–328
- Rougee A, Picard CL, Troussset YL, et al. (1993) Geometrical calibration for 3D X-ray imaging. In: *Medical Imaging 1993: Image Capture, Formatting, and Display*. Newport Beach, CA, pp 161–169
- Rührnschopf E-P, Kalender W (1981) Artifacts caused by non-linear partial volume and spectral hardening effects in computerized tomography. *Electromedica* 2:96–105
- Saint-Felix D, Troussset Y, Picard C, et al. (1994) In vivo evaluation of a new system for 3D computerized angiography. *Phys Med Biol* 39:583–595
- Siewerdsen JH, Jaffray DA (2001) Cone-beam computed tomography with a flat-panel imager: Magnitude and effects of X-ray scatter. *Med Phys* 28:220–231
- Siewerdsen JH, Daly MJ, Bakhtiar B, et al. (2006) A simple, direct method for X-ray scatter estimation and correction in digital radiography and cone-beam CT. *Med Phys* 33:187–197
- Soederman M, Babic D, Homan R, et al. (2005) Three-dimensional roadmap in neuroangiography: Technique and clinical interest. *Neuroradiology* 47:735–740
- Sourbelle K, Kachelriess M, Kalender W (2005) Reconstruction from truncated projections in CT using adaptive detrunctation. *Eur Radiol* 15:1008–1014
- Spahn M, Strotzer M, Voelk M, et al. (2000) Digital radiography with a large-area, amorphous-silicon, flat-panel X-ray detector system. *Invest Radiol* 35:260–266
- Starman J, Pelc N, Strobel N, et al. (2005) Estimating 0th and 1st moments in C-arm CT data for extrapolating truncated projections. In: *Medical Imaging 2005: Image Processing*. San Diego, CA, pp 378–387
- Sugahara T, Korogi Y, Nakashima K, et al. (2002) Comparison of 2D and 3D digital subtraction angiography in evaluation of intracranial aneurysms. *Am J Neuroradiol* 23:1545–1552
- Sze DY, Strobel N, Fahrig R, et al. (2006) Transjugular intrahepatic portosystemic shunt creation in a polycystic liver facilitated by hybrid cross-sectional/angiographic imaging. *J Vasc Intervent Radiol* 17:711–715
- Tu RK, Cohen WA, Maravilla KR, et al. (1996) Digital subtraction rotational angiography for aneurysms of the intracranial anterior circulation: injection method and optimization. *Am J Neuroradiol* 17:1127–1136
- United Nations Scientific Committee on the Effects of Atomic Radiation (UNSCEAR) (2000) Sources and effects of ionizing radiation, vol II: Effects. In: Report to the General Assembly, with scientific annexes. United Nations, Geneva New York
- van den Berg JC, Overtom TTC, de Valois JC, et al. (2002) Using three-dimensional rotational angiography for sizing of covered stents. *Am J Roentgenol* 178:149–152
- Virmani S, Ryu RK, Sato KT, et al. (2007) Effect of C-arm angiographic CT on transcatheter arterial chemoembolization of liver tumors. *J Vasc Intervent Radiol* 18:1305–1309
- Wallace MJ, Murthy R, Kamat PP, et al. (2007) Impact of C-arm CT on hepatic arterial interventions for hepatic malignancies. *J Vasc Intervent Radiol* 18:1500–1507
- Wiesent K, Barth K, Navab N, et al. (2000) Enhanced 3-D-reconstruction algorithm for C-arm systems suitable for interventional procedures. *IEEE Transact Med Imaging* 19:391–403
- Yamazaki T, Tamura T, Nokita M, et al. (2004) Performance of a novel 43-cm × 43-cm flat-panel detector with CsI:Tl scintillator. In: *Medical Imaging 2004: Physics of Medical Imaging*. San Diego, CA, pp 379–385
- Zellerhoff M, Scholz B, Rührnschopf EP, et al. (2005) Low contrast 3D reconstruction from C-arm data. In: *Medical imaging 2005: Physics of medical imaging*. SPIE, San Diego, CA, pp 646–655
- Zhu L, Bennett NR, Fahrig R (2006) Scatter correction method for X-ray CT using primary modulation: Theory and preliminary results. *IEEE Transact Med Imaging* 25:1573–1587